

# Dynamic Simulator for HTV Capture with Space Station Remote Manipulator System

Ryo YOSHIMITSU\*, Yudai YUGUCHI\*, Akinori KOBAYASHI\*, Riku TAKANO\*, Kenji NAGAOKA\*, Kazuya YOSHIDA\*, Satoko ABIKO\*, Hiroki NAKANISHI†, Mitsushige ODA†, and Hiroshi UENO§

\*Tohoku University, 6-6-01, Aramaki Aoba, Aoba-ku, Sendai, Miyagi 980-8579, Japan  
e-mail: { yoshimitsu, yuguchi, a-kobayashi, takano, nagaoka, yoshida } @astro.mech.tohoku.ac.jp  
abiko@space.mech.tohoku.ac.jp

†Tokyo Institute of Technology, 2-11-1, Ookayama, Meguro-ku, Tokyo 152-8550, Japan  
e-mail: nakanishi.hiroki@mes.titech.ac.jp  
oda.m.ab@m.titech.ac.jp

§Japan Aerospace Exploration Agency, 3-1-1, Yoshinodai, Chuo-ku, Sagami-hara, Kanagawa  
252-5210, Japan  
e-mail: ueno.hiroshi@jaxa.jp

## Abstract

This paper presents a dynamic simulator with a contact model for capture operations using a large space manipulator. Capture operations in orbit have commonly used enclosed wires. The contact dynamics between the wires and the target generate complicated motion that is difficult to predict. Additionally, the joint flexibility of the manipulator makes capture operations more difficult. For these reasons, there is a potential risk, and such missions, which require a high degree of safety, may be endangered. In this study, we developed a simulator for capturing a target in orbit with joint flexibility and contact dynamics. An empirical equation for the contact dynamics with a wire was derived, and the performance of the simulator was evaluated by parameter matching with a flight data. Finally, a case study was conducted, and an example of the risk was developed.

## 1 Introduction

On-orbit transportation is necessary technology for activity on the International Space Station (ISS). The H-II Transfer Vehicle (HTV), which was developed by the Japan Aerospace Exploration Agency (JAXA), is currently responsible for one of the transportation means (Figure 1). HTV-4 was launched on August 4, 2013, and transported essential materials to the ISS. The retirement of NASA's space shuttles has accelerated demand for the HTV. The HTV is docked with the ISS using the Space Station Remote Manipulator System (SSRMS). The SSRMS, which is a large flexible space manipulator with



Figure 1. HTV captured by SSRMS ©NASA

seven degrees of freedom, can capture and guide the HTV. In addition, the SSRMS can be used to build large space structures, such as the ISS, and assist astronauts during extra-vehicular activities. Thus, capture operations by the SSRMS play important roles in on-orbit service. When carrying out these space activities, the SSRMS needs to capture a target.

To capture the HTV, the SSRMS is equipped with a dedicated holding mechanism called the Latching End Effector (LEE). The LEE has three snare wires that form a curvilinear triangle in the cylinder of the end effector. The HTV is equipped with a Grapple Fixture (GF) that vertically extends from the HTV and can be captured by the LEE. Figure 2 shows an overview of the LEE and the GF. In the capture sequence shown in Figure 3, (a) the operator first guides and inserts the SSRMS to cage the tip of the GF in the curvilinear wire triangle of the LEE. Subse-

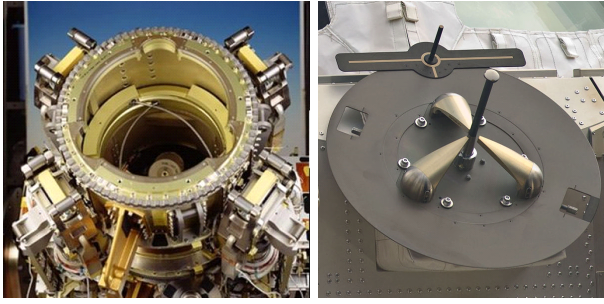


Figure 2. LEE and GF ©NASA

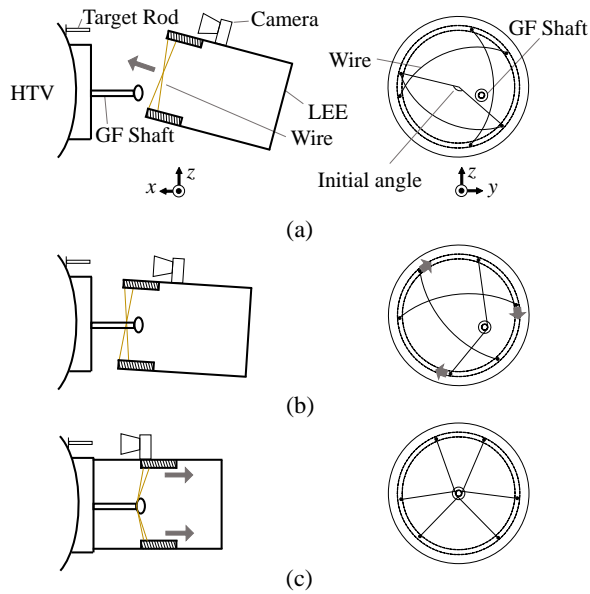


Figure 3. HTV capture sequence by LEE

quently, (b) the GF is latched by narrowing the triangle of the wires. Note that the operator sees a target rod on the GF through a camera of the LEE but cannot observe the size of the narrowing curvilinear triangle and the contact point between the wires and the GF. Finally, (c) the LEE and the GF are constrained geometrically owing to the wires fully tightening and are docked by the wires drawing the GF into the cylinder of the LEE. This capture method using the LEE and the GF has been commonly used in orbit, however, its secure operation depends greatly on the skill of the operator. In general, the capture operation involves difficult operational techniques and a high level of training because the operator cannot observe the contact point and because the SSRMS cannot completely stop before holding the GF, owing to the joint flexibility of the SSRMS. Furthermore, in a microgravity environment, the contact phenomenon is quite complicated, and it can be subject to high risk even with a weak contact force. The potential risks need to be known to avoid a deadly accident. Therefore, the contact phenomenon must be examined.

We have therefore developed a dynamic simulator that be used to evaluate and analyze the capture operations quantitatively. The simulator is intended for use in determining the potential risks described above and in the training of the operator. Roman Tutor [1], a simulator that is related to the SSRMS simulator, is also used in training astronauts to operate the SSRMS. However, in Roman Tutor, the contact dynamics are not modeled. Despite the existence of Roman Tutor, there has not been much examination of the contact between a wire and the GF. Therefore, we have studied these contact dynamics in [2], [3]. However, these studies did not confirm consistency with the on-orbit dynamics.

In this study, we developed a dynamic simulator for use in simulating capture of the HTV by the SSRMS. An overview of the simulator is presented in section 2. The joint flexibility model of the SSRMS, which is needed to finely simulate on-orbit dynamic behavior, is presented in section 3. The contact dynamics are described in section 4. Section 5 describes how reasonable values were determined for simulation parameters to match behavior in the simulator with the flight data. Finally, an example of the risk is presented through a case study in section 6.

## 2 HTV Capture Simulator

Figure 4 shows the LEE and the GF in the simulator. The LEE and the GF are modeled based on their actual size, and the wire curve in the LEE is described by using an elliptic function. Figures 5 and 6 show an overview of the HTV capture simulator and its GUI display, respectively. The LEE and the GF, as well as the dynamic model of the HTV, use actual values. The dynamic model of the SSRMS is presented in the following section. In practice, an astronaut operates two joysticks and watches the monitor. Therefore, this simulator reproduces the interface actually used. In addition, the display is designed to make conducting the contact analysis and the case study easy. The partitions in the display represent the following:

- i. The relative position and velocity between the LEE and the GF and the joint angle and velocity
- ii. The values for determining the contact position between the wire and the GF to conduct the case study
- iii. Buttons for changing the camera position
- iv. Buttons for changing the control mode of the SSRMS
- v. Buttons for initializing, starting, and stopping the simulation
- vi. A monitor for the viewing the simulation graphics (The view angle can be changed by the camera position button)
- vii. A simulation time display
- viii. A power gauge for the joystick inputs

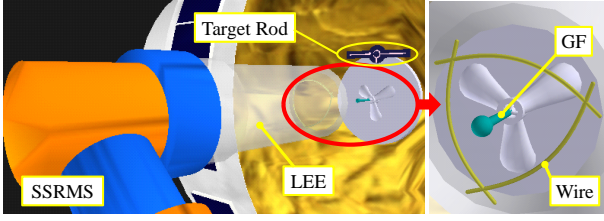


Figure 4. Illustration of LEE and GF in simulator

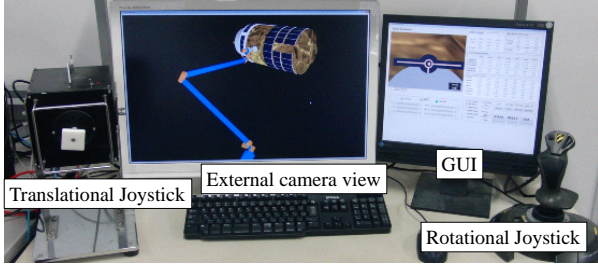


Figure 5. Overview of HTV capture simulator

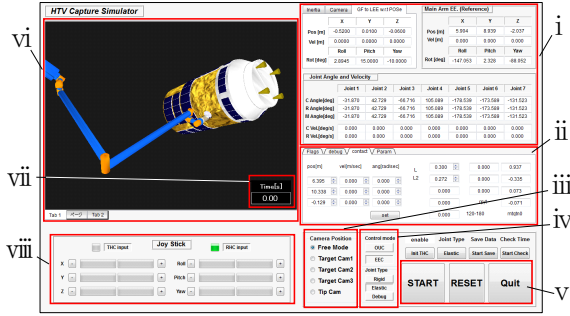


Figure 6. Simulator display

### 3 Dynamics of SSRMS

#### 3.1 Nonlinear characteristic of joints

In depicting the motion of the SSRMS, the simulator considers the geometric connection relations of the joints and the nonlinear stiffness of the joint. The geometric connection relations are constructed based on Figure 7 and Table 1 [4]. Each link of the SSRMS is represented by frame, as shown Figure 7. In Table 1,  $m_i$  represents the mass of link  $i$ ;  $c_i$  and  $I_i$  represent the mass center location vector in each link frame and the inertia moment matrix of the mass center, respectively; and  $p_{i,i+1}$  represents the position vector that expresses the  $i+1$  joint location in link frame  $i$ .

Each joint of the SSRMS has nonlinear flexibility owing to low stiffness. As described in [4], based on ground tests and on-orbit data, and neglecting hysteresis, the joint characteristics can be represented by the following nonlinear function  $g(\delta_m)$ :

$$\tau_g = \text{sign}(\delta_m)g(\delta_m) \quad (1)$$

$$g(\delta_m) = \begin{cases} \frac{\tau_\Delta}{\Delta^2} \delta_m^2 & |\delta_m| \leq \Delta \\ K_g(|\delta_m| - \Delta) + \tau_\Delta & \text{otherwise} \end{cases} \quad (2)$$

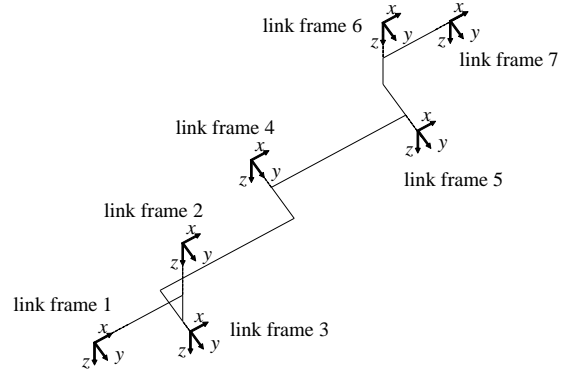


Figure 7. Joint connectivity of SSRMS

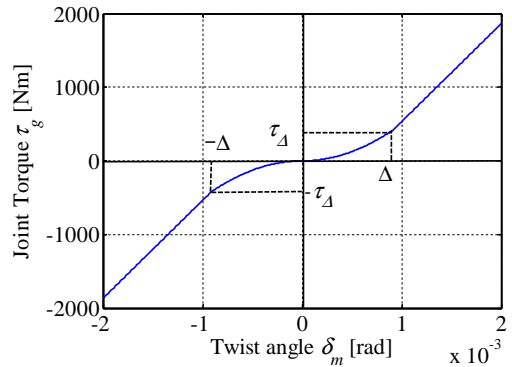


Figure 8. Joint characteristic of SSRMS

where  $K_g = 1.33 \times 10^6$  [Nm/rad],  $\Delta = 9.17 \times 10^{-4}$  [rad],  $\tau_\Delta = 434.5$  [Nm], and the twist angle  $\delta_m$  is defined as the motor angle minus the link angle. All joints have the same characteristics, illustrated in Figure 8.

#### 3.2 Modeling of flexible manipulator

We modeled the joint flexibility of the space manipulator using a 2-inertia system [5]. The 2-inertia system gives a virtual joint in which each joint has two masses with a rigid link and a rotary motor. These are connected by a linear torsional spring that generates elasticity by the coupling effect. In this case, because a gear reducer behaves like a spring element, we used a model that could describe the inertia of a link and an actuator. Therefore, the motion of the SSRMS can be represented by solving the following two simultaneous equations of motion for the manipulator and the motor:

$$M_a(q_a)\ddot{q}_a + C(q_a, \dot{q}_a) - \tau_g(\delta_m) = J_e^T \mathcal{F}_e \quad (3)$$

$$M_m\ddot{q}_m + D\dot{q}_m + \tau_g(\delta_m) = \tau_c \quad (4)$$

where

$q_a \in \mathbb{R}^{7 \times 1}$  : the angle of the actual joint axis

$q_m \in \mathbb{R}^{7 \times 1}$  : the angle of the motor axis

Table 1. Inertial properties of SSRMS [4]

$i$	1	2	3	4	5	6	7	8
$m_i$ [kg]	246.66	105.98	105.98	314.88	279.2	105.98	105.98	243.66
$c_i$ [m]	0.669	0	0	3.55	3.55	0	0	0.669
	0	0	-0.2316	-0.08	0	-0.337	0	0
	0	0.2983	0	0	0	0	-0.404	0
$I_i$ [kgm <sup>2</sup> ]	$I_{xx} = 9.336$ $I_{yy} = 44.413$ $I_{zz} = 44.413$ $I_{xy} = 0$ $I_{yz} = 0$ $I_{zx} = 0$	$I_{xx} = 12.19$ $I_{yy} = 12.13$ $I_{zz} = 3.061$ $I_{xy} = 0$ $I_{yz} = 0$ $I_{zx} = 0$	$I_{xx} = 8.088$ $I_{yy} = 3.061$ $I_{zz} = 8.446$ $I_{xy} = 0$ $I_{yz} = 0$ $I_{zx} = 0$	$I_{xx} = 15.41$ $I_{yy} = 2094.71$ $I_{zz} = 2103.19$ $I_{xy} = 49.52$ $I_{yz} = 0$ $I_{zx} = 0$	$I_{xx} = 9.522$ $I_{yy} = 1966.28$ $I_{zz} = 1966.28$ $I_{xy} = -39.95$ $I_{yz} = 0$ $I_{zx} = 0$	$I_{xx} = 8.305$ $I_{yy} = 3.061$ $I_{zz} = 8.386$ $I_{xy} = 0$ $I_{yz} = 0$ $I_{zx} = 0$	$I_{xx} = 12.13$ $I_{yy} = 12.13$ $I_{zz} = 3.061$ $I_{xy} = 0$ $I_{yz} = 0$ $I_{zx} = 0$	$I_{xx} = 9.336$ $I_{yy} = 44.41$ $I_{zz} = 44.41$ $I_{xy} = 0$ $I_{yz} = 0$ $I_{zx} = 0$
$p_{i,i+1}$ [m]	1.3589	0	0	7.11	7.11	0	0	1.3589
	0	0	-0.5692	-0.475	0	-0.5692	0	0
	0	0.7026	0	0	0	0	-0.7026	0

$M_a \in \mathbb{R}^{7 \times 7}$  : the inertia matrix of the SSRMS

$M_m \in \mathbb{R}^{7 \times 7}$  : the inertia matrix of the motor

$C \in \mathbb{R}^{7 \times 1}$  : the nonlinear velocity-dependent term of the SSRMS

$D \in \mathbb{R}^{7 \times 1}$  : the viscous damping coefficient of the motor

$\mathcal{F}_e \in \mathbb{R}^{6 \times 1}$  : the force and moment exerted on the end-effector

$J_e \in \mathbb{R}^{6 \times 7}$  : the Jacobian matrix with respect to the end-effector

$\tau_c \in \mathbb{R}^{7 \times 1}$  : the torque vector on the joints

$\delta_m \in \mathbb{R}^{7 \times 1}$  : the twist angle vector between the motor and the link

$\tau_g \in \mathbb{R}^{7 \times 1}$  : the gearbox torque vector with respect to the twist angle vector

The inertia matrix of the motor is represented as follows in [4]:

$$M_m = \begin{bmatrix} I_{zz}\eta^2 & 0 & \cdots & 0 \\ 0 & I_{zz}\eta^2 & \cdots & 0 \\ \vdots & \vdots & \ddots & \vdots \\ 0 & 0 & \cdots & I_{zz}\eta^2 \end{bmatrix} \quad (5)$$

where  $I_{zz} = 2.67 \times 10^{-4}$  [kgm<sup>2</sup>] denotes the inertia moment and  $\eta = 1845$  denotes the gear reduction ratio. The value of the viscous damping coefficient of the motor was determined by means of parameter matching with the flight data.

### 3.3 Control method

While operating the SSRMS, the operator observes a relative position with respect to the GF only through the camera on the LEE. Therefore, the SSRMS in the simulator should be operated using the camera coordinate system rather than the inertial coordinate system. For this reason,

letting  $J_c(q_a)$  be a Jacobian matrix for the camera coordinate system, the desired joint angular velocity vector  $\dot{q}_a^d$  is derived as shown:

$$\dot{q}_a^d = J_c(q_a)^+ \begin{bmatrix} v_e^d \\ \omega_e^d \end{bmatrix} \quad (6)$$

where  $[v_e^{dT} \ \omega_e^{dT}]^T$  denotes the desired velocity of the end-effector for the camera coordinate system because the operator determines the desired value from joysticks,  $(\cdot)^+$  operator denotes the pseudo inverse of a matrix. The desired joint angle vector  $q_a^d$  is derived as the integral of  $\dot{q}_a^d$ , and the joint torque  $\tau_c$  is given by the following PD controller:

$$\tau_c = k_p(q_a^d - q_a) + k_d(\dot{q}_a^d - \dot{q}_a) \quad (7)$$

where  $k_p$  and  $k_d$  represent the proportional and derivative gain matrices, respectively, and which are determined by parameter matching.

## 4 Contact dynamics between wire and GF

This section describes the contact dynamics between a wire and the GF. Because the shape of a wire-applied force changes with time, as shown Figure 9, contact dynamics between a wire and the GF are complicated, in contrast to rigid body contact. Therefore, the simulator must finely duplicate dynamic behavior attributed a contact reaction force. In general, a contact force can be divided into a normal force  $F_n$  and a frictional force  $F_f$ . The normal force  $F_n$  is defined as the linear sum of kinetic and static elements, i.e.,  $F_n = F_k(\delta) + F_s(\delta)$ . Let  $k$  be the stiffness and  $c$  be the viscous damping. The normal force  $F_n$  can be expressed as a function of the displacement of penetration  $\delta$  [6]:

$$F_n = c\delta^p \dot{\delta}^q + k\delta^n \quad (8)$$

where  $p$ ,  $q$ , and  $n$  are constant values. When  $p = 0$  and  $q = n = 1$ , this model represents the following spring-

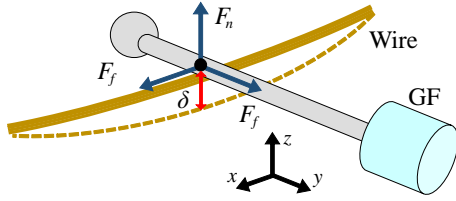


Figure 9. Contact model between wire and GF

dashpot model:

$$F_n = c\dot{\delta} + k\delta \quad (9)$$

We have focused on the contact dynamics between a wire and the GF to capture the HTV safely. Eq. (9) was selected as the contact dynamics model in [2], assuming that a wire is modeled as the superposition of a beam and a string and that its stiffness  $k$  can be defined by the ratio of their stiffnesses. The static force model used in [2] is, however, insufficient to express the contact kinematics between a wire and the GF. A wire would not become a perfectly rigid body during penetration because it is deformed geometrically by contact with the GF. In addition, tension was assumed to be applied to the straight shape of the wire. However, a wire has no tension initially, and in practice, the displacement of the GF is started from a bowed state. In [3], these assumptions were improved based on the results of ground experiments. The results showed that the force observed was greater than that predicted by the simple spring-dashpot model and that it can be approximated by a quadratic function of the following form:  $F_n(\delta) = A\delta^2 + B\delta + C$ .

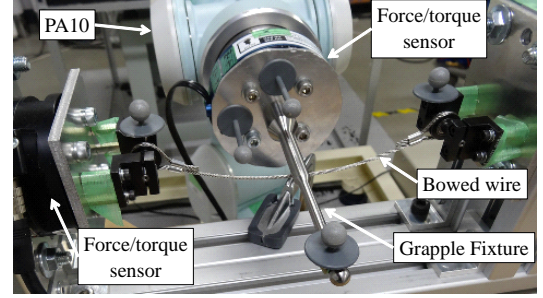
For further study, other factors need to be considered as well. In the previous experiments mentioned, the load was applied in the direction perpendicular to the ground plane, and the reaction force was distributed laterally. In addition, given the limited amount of experimental data obtained less, an approximate equation was obtained by based only on the discrete response. To derive a more realistic and precise static force equation, we carried out further experiments.

#### 4.1 Experimental conditions

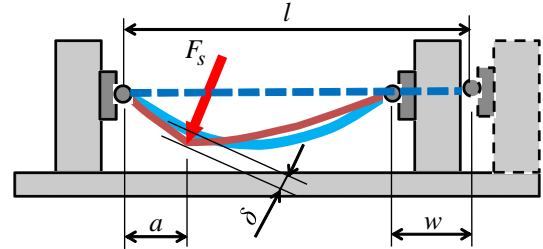
In our experiment, a device that fixes both ends of a wire was set in a rigid frame. The wire used in the experiment is thinner and more flexible than the actual wire on the LEE. An overview and a schematic view of the experimental devices are shown in Figures 10 (a) and (b), respectively. Both of the end points of the wire are rotation points fixed by idlers. This device is equipped with a slide mechanism for setting the horizontal displacement of the end point of the wire. To measure the force, the end point is equipped with a force/torque sensor produced by Nitta Corporation (IFS-90M31A 50-I 50). To apply the load to a wire, we used a PA10 industrial robotic arm produced by Mitsubishi Heavy Industry. The tip of the PA10 is also

Table 2. Wire configuration in the experiments

Length $l$	180 mm
Diameter	2 mm
Horizontal displacement $w$	0, 5, 10 mm
Contact position $a$	70, 80, 90, 100, 110 mm (from the left end)



(a) Overview



(b) Schematic view

Figure 10. Experimental setup for analysis of the contact dynamics

equipped with a force/torque sensor (IFS-90M31A 50-I 50) and a rod that represents the GF. In the experiments, we measured the reaction force of the wire with respect to the bending displacement during static loading applied to the bowed wire by the PA10. There was no frictional force because the force was applied to the bowed wire vertically. An OptiTrack FLEX:V100R2 motion capture system produced by NaturalPoint was used to measure the displacement  $\delta$ . The experimental conditions for the wire are presented in Table 2. Note that of the contact positions between the wire and the rod listed in Table 2, the 90 mm position is at the center of the wire.

#### 4.2 Experimental results

The graphs shown in Figure 11 illustrate the relationship between the displacement  $\delta$  and the static reaction force  $F_s$  for each condition. These graphs show that the stiffness of the static reaction force  $F_s$  increases because a dominant factor changes with the displacement  $\delta$ . In the cases of the 5 mm and 10 mm horizontal displacements in particular, the stiffness change was remarkable. The stiffness then started to change linearly as the wire extended to a certain extent and reached a stable value. Moreover, the stiffness did not change when the horizontal displace-

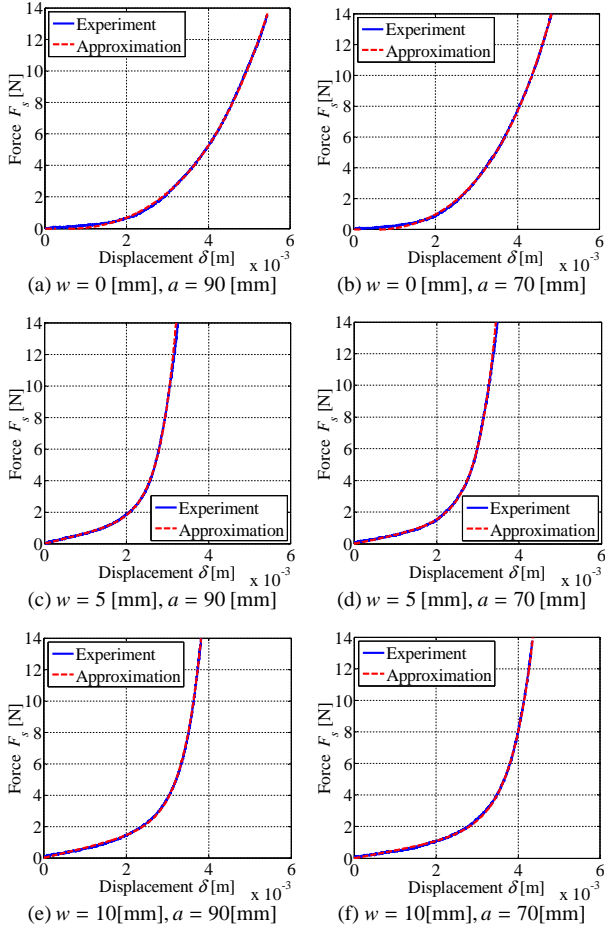


Figure 11. Experimental measurements of wire stiffness

ment exceeded over 5 mm. Therefore, we conclude that the static reaction force can be regarded as a superposition of two functions.

Based on these results, we selected the following an empirical equation:

$$F_s(\delta) = \alpha(e^{\beta\delta} - 1) + \gamma\delta \quad (10)$$

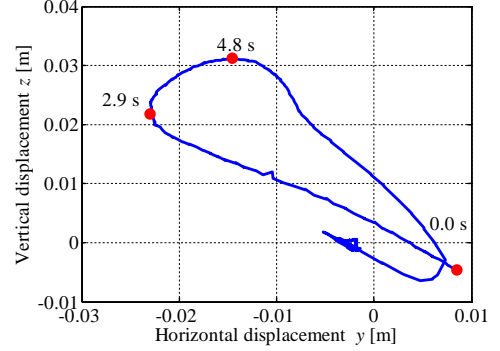
where  $\alpha$ ,  $\beta$ , and  $\gamma$  represent arbitrary constant parameters. The graphs made using Eq. (10) are shown together in Figure 11 and show that Eq. (10) represents the stiffness change of the wire well.

Considering the characteristic of Eq. (10), constant values for the kinetic element of the normal force  $F_k(\delta)$  in the simulator were set as  $p = 2$  and  $q = 1$ , and the frictional force  $F_f$  applied was represented by the Coulomb friction model, as shown below:

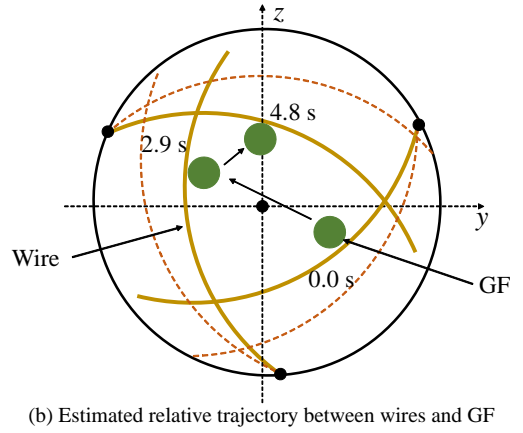
$$F_k = c\delta^2\dot{\delta} \quad (11)$$

$$F_f = \mu F_n \quad (12)$$

where  $\mu$  denotes the coefficient of kinetic friction.



(a) Trajectory from telemetry data on y-z plane



(b) Estimated relative trajectory between wires and GF

Figure 12. Trajectory of telemetry and estimation

## 5 Parameter matching of simulator

This section presents the matching of the undetermined parameters to precisely incorporate the SSRMS motion and the contact dynamics in the simulator. In the matching process, we utilized the flight data used in [7], which was estimated from the practical telemetry data of the sensor output of the HTV and the camera images on the LEE and the ISS.

### 5.1 Relative trajectory between wires and GF

In determining the values of the parameters of interest, it is important to estimate where the GF contacts the wire in the LEE, because the contact point is not filmed by the camera. Hence, we first analyzed how far the GF was moving with respect to the wires, using both the flight data and the captured movie. Figure 12 (a) represents the results plotted as a trajectory on the y-z plane from 0 s to 20 s in the flight data. As Figure 12 (a) shows, the GF started moving from the lower right to the upper left of the curvilinear triangle at 0 s and made contact at 2.9 s and 4.8 s, respectively. In addition, the GF being fixed by the wires can be represented by drawing a circular trajectory inside a curvilinear triangle. Because the GF follows such

Table 3. Initial states of SSRMS and tightening values of wire

SSRMS	Initial joint angle [°] (based on Figure 7)	-31.87
		42.73
		-66.72
		105.1
Initial relative position vector [m]	Initial relative velocity vector [m/s]	-178.6
		-174.6
		-131.5
		-0.4760
Initial relative attitude vector [°]	Initial relative velocity vector [m/s]	0.013
		-0.003
		0.030
		-0.012
wire	initial angle [°]	0.008
		0.0108
		0.763
wire	final angle [°]	0.110
		130
		200
wire	tightening time [s]	5

Table 4. Simulation parameter values obtained by matching with flight data

$\alpha$	$\beta$	$\gamma$	$c$ [kgs/m <sup>2</sup> ]	$\mu$
0.0043	2162.2	648.6	$0.83 \times 10^7$	0.08
$k_{p,i}$ [Nm/rad]	$k_{d,i}$ [Nms/rad]	$D_{ii}$ [Nms/rad]		
120	240	18000		

a trajectory, we estimated that the GF moved as shown in Figure 12 (b).

## 5.2 Result of parameter matching

When matching the behavior in the simulator with the flight data, the contact force between the wire and the GF was based on the empirical equation though the material of the wire used in the experiment differs. In addition, the initial states of the SSRMS were set to be the same as in the flight data. The tightening time, which is the moving rate of the end point of the wire from the initial angle to the final angle, also uses the same values. These conditions are summarized in Table 3. The values of the parameters for the wire reaction force  $\alpha, \beta, \gamma, c, \mu$ , the control gain of the SSRMS  $k_p, k_d$  and viscous damping coefficient of the motor  $D$  were determined by parameter matching.

The result of the parameter matching is shown in Figures 13 and 14. Figure 13 shows the time response of the simulator behavior and the flight data. Figure 14 shows successive pictures of the simulator. The simulation parameter values obtained by matching with the flight data presented in Table 4. Figures 13 and 14 illustrate the trends of the estimation shown in Figure 12, however the simulator behavior has higher amplitude than the flight

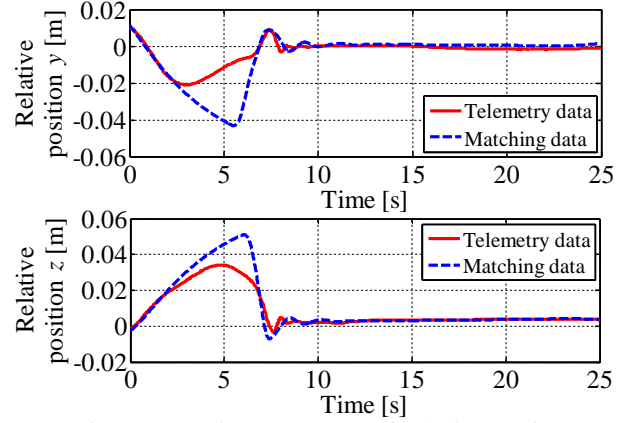


Figure 13. Time response of relative position between LEE and GF

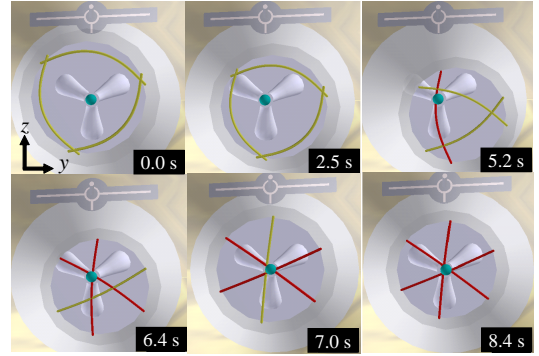


Figure 14. Successive pictures of capture sequence

data. We considered that higher amplitude could be tolerated as the wide margin because the purpose developing the simulator analyzes the safeness of capture operations. Notice that the values in Table 4 do not ensure uniqueness of the combination of parameters because the number of parameters is large and uncertainly factor may be included. However, in terms of matching the flight data, the numerical model simulates the relative motion of capture operation.

## 6 Case Study

This section describes a case study conducted examine the safeness of capturing the HTV. When an astronaut operates a large space manipulator and captures a target using the LEE, the criteria for the capture possibility are defined to be whether the mission can be safely accomplished. If this criteria are not satisfied, a capture sequence must be stopped immediately. The relative position and angle in the approaching phase before the contact are defined as part of the assessment that the criteria can be met, but the relative translational and rotational velocity are not defined explicitly. Therefore, the margin of safety of the capture velocity with respect to the SSRMS operation velocity needs to be examined.

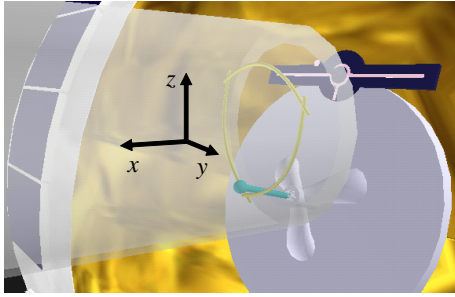


Figure 15. Initial state of case study

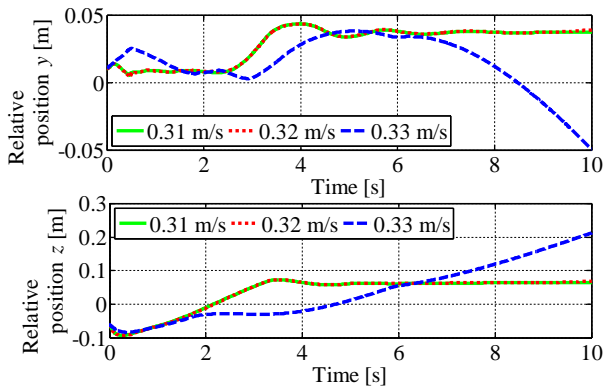


Figure 16. Results of case study

## 6.1 Case study results and discussion

We conducted a case study under the following conditions.

- The matching parameters listed in Table 4 were used.
- The case study was started from the state at which the GF was inserted into the enclosed region of the LEE.
- In the worst case, the GF was located in a corner of the enclosed region, as shown Figure 15.
- The curvilinear triangle began narrowing at 0 s.

In addition to the above conditions, the LEE was supplied with an initial velocity in the  $z$ -axis direction. We then determined the limiting initial velocity at which the GF and the LEE could be constrained.

The results are shown in Figure 16. When the initial velocity was less than 0.32 m/s, the LEE captured the GF because the relative velocity between the two was 0 m/s. However, when the initial velocity was greater than 0.33 m/s, the LEE failed to capture the GF. Therefore, for this case study, the limiting initial velocity was found to be 0.32 m/s. This velocity is much greater than the typical operating velocity of the SSRMS, which is 0.03 m/s.

## 7 Conclusions

This paper describes a dynamic simulator for the HTV capture by the SSRMS. This simulator was devel-

oped to analyze safe capture operations and is therefore focused on joint flexibility and the contact dynamics between a wire and the GF. An empirical equation that represents the contact dynamics was introduced based on the results of ground experiments and was integrated into the simulator to match its behavior with available flight data. The simulator can contribute to the analysis of the safety of capture conditions, as demonstrated by the case study presented in this paper. The potential risks inherent in the capture operation will be gradually clarified by conducting additional case studies.

## Acknowledgment

We would like to express thanks to the JAXA HTV project team that provided us with the telemetry data needed to carry out this research.

## References

- [1] K. Belghith, R. Nkambou, F. Kabanza, and L. Hartman. An Intelligent Simulator for Telerobotics Training. *IEEE Transactions on Learning Technologies*, 5(1):11–19, 2012.
- [2] N. Uyama, K. Yoshida, H. Nakanishi, M. Oda, H. Sawada, and S. Suzuki. Contact Dynamics Modeling for Snare Wire Type of End Effector in Capture Operation. *Transactions of The Japan society for Aeronautical and Space Sciences, Aerospace Technology Japan*, 10(ists28):Pd.77–Pd.84, 2012.
- [3] S. Abiko, N. Uyama, T. Ikuta, K. Nagaoka, K. Yoshida, H. Nakanishi, and M. Oda. Contact Dynamics Simulation for Capture Operation by Snare Wire Type of End Effector. In *Proceedings of the 11th International Symposium on Artificial Intelligence, Robotics and Automation in Space*, 03b-02, 2012.
- [4] S. B. Skaar and C. F. Ruoff. *Teleoperation and robotics in space*, volume 161 of *Progress in Astronautics and Aeronautics*. AIAA, 1994.
- [5] M. W. Spong. Modeling and Control of Elastic Joint Robots. *Journal of Dynamic Systems, Measurement, and Control*, 109:310–319, 1987.
- [6] G. Gilardi and I. Sharf. Literature survey of contact dynamics modelling. *Mechanism and machine theory*, 37(10):1213–1239, 2002.
- [7] H. Nakanishi, M. Oda, and S. Suzuki. The Motion Analysis of the HTV Capture with the Space Station Remote Manipulator System (SSRMS). In *Proceedings of the 2012 JSME Conference on Robotics and Mechatronics*, 1A2-J07, 2012. (in Japanese).